



Strain Evolution in Lithium Manganese Oxide Electrodes

Ö.Ö. Çapraz^{1,2,3} · S. Rajput^{1,2} · S. White^{2,3} · N.R. Sottos^{1,2}

Received: 1 August 2017 / Accepted: 5 February 2018 / Published online: 22 February 2018

© Society for Experimental Mechanics 2018

Abstract

Lithium manganese oxide, LiMn_2O_4 (LMO) is a promising cathode material, but is hampered by significant capacity fade due to instability of the electrode-electrolyte interface, manganese dissolution into the electrolyte and subsequent mechanical degradation of the electrode. In this work, electrochemically-induced strains in composite LMO electrodes are measured using the digital image correlation (DIC) technique and compared with electrochemical impedance spectroscopy (EIS) measurements of surface resistance for different scan rates. Distinct, irreversible strain variations are observed during the first delithiation cycle. The changes in strain and surface resistance are highly sensitive to the electrochemical changes occurring during the first cycle and correlate with prior reports of the removal of the native surface layer and the formation of cathode-electrolyte interface layer on the electrode surface. A large capacity fade is observed with increasing cycle number at high scan rates. Interestingly, the total capacity fade scales proportionately to the strain generated after each lithiation and delithiation cycle. The simultaneous reduction in capacity and strain is attributed to chemo-mechanical degradation of the electrode. The *in situ* strain measurements provide new insight into the electrochemical-induced volumetric changes in LMO electrodes with progressing cycling and may provide guidance for materials-based strategies to reduce strain and capacity fade.

Keywords Cathode-electrolyte Interface · Strain measurement · Lithium manganese oxide · Deformation · Surface reactions

Introduction

The electrochemical performance of a lithium ion battery is highly coupled to the mechanical response of the electrode materials [1–3]. During repeated charge and discharge cycles of the battery, Li ions move in and out of the active electrode materials, causing volumetric expansion and contraction. Complex electrochemical reactions also occur during cycling, which lead to the formation of surface products that influence strain development as well as battery performance, particularly in the first cycle [4–9]. Since the electrode materials in a battery cell are constrained by a current collector and other

packaging, significant stresses develop and ultimately can cause electrode fracture and debonding [10–12].

The electrochemically-induced stress and strain development in high capacity anode materials has been the subject of much investigation [3]. In particular, digital image correlation has become a prominent tool for characterizing *in situ* strains during electrochemical cycling. Qi et al. used digital image correlation to measure deformation and strain fields in composite graphite electrode harvested from commercial batteries [13]. Jones et al. investigated electrochemically-induced deformation mechanisms in the free-standing composite graphite electrodes using digital image correlation [1, 6, 14]. Gonzalez et al. used X-ray micro computed tomography to visualize the microstructural evolution of silicon composite electrodes during the initial lithiation [15]. Deformation in cathode materials was investigated by Eastwood et al. using 3D X-ray computed tomography to characterize dilation and motion of manganese oxide particles [16].

The need to understand the coupled electro-chemical-mechanical response in cathode materials is even more critical for the development of high performance Li-ion batteries. In general, electrochemically-induced volume changes are much lower in cathode materials compared to anode materials.

✉ N. R. Sottos
n-sottos@illinois.edu

¹ Department of Material Science and Engineering, University of Illinois at Urbana-Champaign, Urbana, IL 61801, USA

² Beckman Institute of Science and Technology, University of Illinois at Urbana-Champaign, Urbana, IL 61801, USA

³ Aerospace Engineering, University of Illinois at Urbana-Champaign, Urbana, IL 61801, USA



However, even small strains in a brittle cathode material can cause damage. Particle fracture and cracks have been observed in layered LiCoO_2 [17], LiNiO_2 [18], spinel LiMn_2O_4 [19] and LiFePO_4 [20] electrodes during cycling.

Spinel lithium manganese oxide, LiMn_2O_4 (LMO), is a promising cathode material for lithium-ion batteries because of its stability, high discharge voltage, environmental safety and low cost [21, 22]. However, LMO cathodes suffer from significant capacity fade with electrochemical cycling due to instability of the surface-electrolyte interface, manganese dissolution into the electrolyte and eventually particle fracture [3, 23, 24].

Electrochemical cycling induces well-known dimensional changes at the atomic level in spinel LMO electrodes. Sun et al. measured variations in lattice parameter with respect to the lithium composition (x) in the spinel $\text{Li}_x\text{Mn}_2\text{O}_4$ [6]. As shown in Fig. 1, the lattice parameter decreases from 8.23 Å to 8.035 Å as lithium ions are removed during delithiation. Upon lithiation, the lattice parameter increases with lithium intercalation into the spinel LiMn_2O_4 structure. Associated with the lattice parameter change, LMO undergoes multiple phase transitions from Cubic I \rightarrow II and II \rightarrow III as the lithium content decreases during delithiation and conversely during lithiation from Cubic III \rightarrow II and II \rightarrow I [25]. Qi et al. has estimated the volumetric expansion of fully lithiated LMO particles as 6.8% from density functional theory [26]. In prior work, we measured 0.4% expansional strain in a free-standing, fully lithiated composite LMO electrode (not adhered to a

current collector). Additionally, the change in strain with respect to the applied voltage in the LMO electrode was well correlated with the changes in the lattice parameter during electrochemical cycling [2].

Reactions between liquid electrolyte and active materials lead to the formation of a surface layer on the electrode that influences strain development. These surface layers are referred to as the solid electrolyte interface (SEI) layer on negative electrodes [4–6], and cathode-electrolyte interface (CEI) layer on positive electrodes [7–9]. Edström et al. [27], Aurbach et al. [28–30], and Eriksson et al. [31, 32] studied formation of CEI layers on the surface of LMO electrodes using different characterization techniques such as X-ray photoelectron spectroscopy, infrared spectroscopy, and Raman spectroscopy. The CEI layer is composed of inorganic compounds (Li_2CO_3 [8, 33], Li_2O [31], LiF [27, 34]), organic compounds (and products from polymerization of organic solvent molecules [35]). Aurbach et al. also reported that there is a native Li_2CO_3 surface layer on the pristine LMO due to reaction between CO_2 in the atmosphere and LMO particles during synthesis [28]. For cathode electrodes, an unstable CEI layer provides ineffective protection to the electrode surface from side reactions with the electrolyte, and enables Mn^{2+} dissolution into electrolyte [27, 31].

Repeated cycling can mechanically deform and damage the surface layer, exposing new active material to the electrolyte. The formation of a rigid surface layer can also mechanically constrain the electrode particles. Tavassol et al. measured significant stress development due to the formation of a surface layer on a model Au electrode [36]. Mukhopadhyay et al. reported that the formation of an SEI layer contributes to irreversible stress in graphite electrodes [3]. Wang et al. [37] and Paz-Garcia et al. [38] also utilized digital image and volume correlation to monitor lithium intercalation-induced strains in silicon electrodes, respectively. Jones et al. measured irreversible strain development associated with SEI formation in composite graphite electrodes [6]. Additionally, Nation et al. [39] and Sheth et al. [40] reported irreversible stress generation during the first delithiation cycle of lithium manganese nickel cobalt oxide and lithium manganese oxide electrodes, respectively. Although there has been extensive discussion of the influence of SEI layers on anode performance, little is known about the effect of the CEI layer on cathodes.

In this paper, we utilize the DIC technique to investigate the effects of CEI formation and cycle rates on strain development in free-standing LMO composite cathodes. In particular, we probe the evolution of irreversible strain during the first cycle, when CEI formation dominates response. We then correlate changes in strain in subsequent cycles with capacity fade at varying scan rates. The use of a free-standing electrode provides a model system for understanding mechanical responses due to electrochemical processes without the constraint of a current collector or battery packaging.

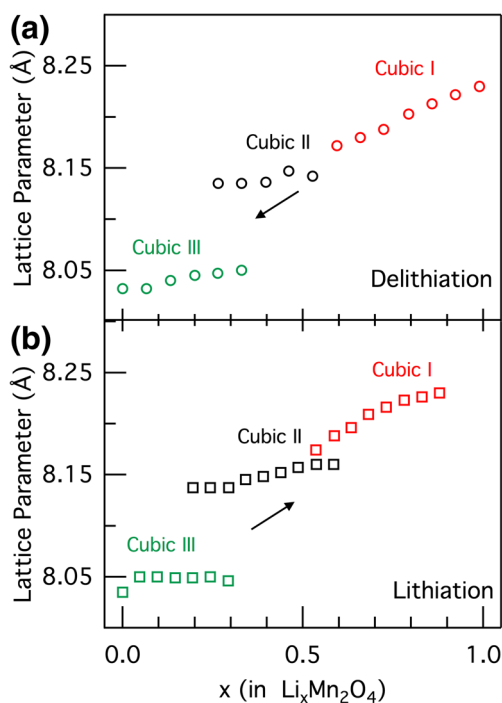


Fig. 1 Phase changes in spinel LMO during lithiation and delithiation. Variation in the cubic lattice parameter as a function of lithium composition (x) in $\text{Li}_x\text{Mn}_2\text{O}_4$ during (a) delithiation, and (b) lithiation between 3.5 and 4.5 V. Arrows indicate direction of the scans. Data is reproduced from x-ray diffraction measurements by Sun et al. [25]



Experimental Procedure

Electrode and Electrolyte Fabrication

LMO electrodes with a composition of 8:1:1 weight ratio of LMO (LiMn_2O_4 , electrochemical grade, Sigma Aldrich), carboxymethyl cellulose sodium salt binder (CMC, Aldrich) and carbon black (Super P Li, Timcal) were fabricated. The CMC polymer binder was dissolved in deionized water in a 1:35 weight ratio. Prescribed amounts of LMO and carbon black were added to the binder solution. The slurry was mixed using a homogenizer (Model 15007ST, Omni) for 1 h at approximately 7500 RPM.

For impedance measurements, the slurry was cast on an aluminum foil current collector using a doctor blade. After drying at room temperature ($\sim 25^\circ\text{C}$) for 24 h, the thickness of the cathode film measured from scanning electron microscope (SEM) images was $7\ \mu\text{m}$. For strain measurements, the slurry was cast onto a copper foil substrate using a doctor blade. After the electrode dried at room temperature for 24 h, it was peeled off from the copper substrate to create a free-stranding electrode. The final LMO electrodes cut to dimension of ca. $3 \times 7\ \text{mm}$.

The electrolyte for all electrochemical testing consisted of ethylene carbonate (EC, Anhydrous, 99%, Sigma Aldrich) and dimethyl carbonate (DMC, Anhydrous, >99%, Sigma Aldrich) by 1:1 volume ratio. 1 M LiPF_6 (98%, Sigma Aldrich) was added to the EC/DMC solution. The electrolyte was mixed with magnetic stirrer in a glove box for 24 h.

Characterization of Surface Morphology

The average LMO particle size distribution was determined from environmental scanning electron microscopy, ESEM (FEI Quanta FEG 450 ESEM), in combination with image analysis (ImageJ, National Institutes of Health). Surface roughness of the LMO electrodes was characterized using a stylus profilometer (Kla Tencor P-6).

Strain Measurements

Strain measurements were carried out in a custom battery half-cell with an optical window (Fig. 2). The cell consists of a stainless steel holder and stainless steel pins for the lithium counter electrode, a polychlorotrifluoroethylene (PCTFE) holder for the working electrode, a stainless steel substrate for the working electrode, PCTFE polymeric support, the PCTFE main body of the cell, substrate bolts for electrical connection and a quartz viewing window. The cell allows for optical access to a nearly unconstrained electrode during electrochemical cycling. A free-standing LMO electrode was spot-welded to a stainless steel substrate in the custom cell. The cell was assembled in a glove box under an argon atmosphere with O_2 and

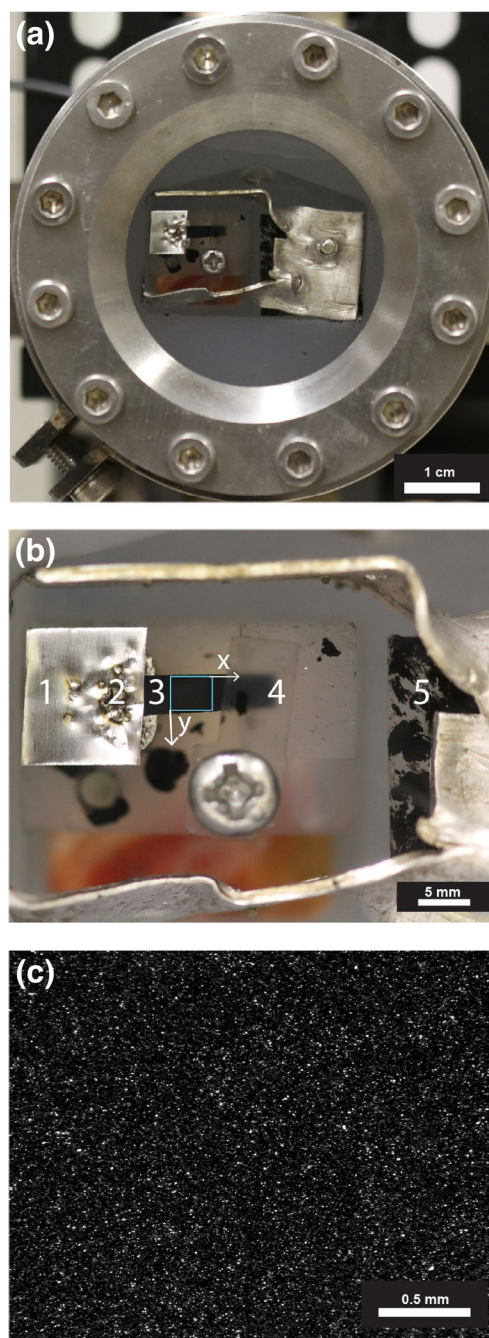


Fig. 2 Images of a custom battery cell and free-standing composite LMO electrode. **(a)** Front view of the custom cell, **(b)** Magnified view of a composite LMO electrode spot-welded on stainless steel. The rectangular box indicates the $2.5 \times 3.0\ \text{mm}$ region of interest for DIC measurements. Numbers indicate (1) polychlorotrifluoroethylene (PCTFE) holder with stainless steel substrate for the working electrode, (2) spot-welding on stainless steel, (3) a composite lithium manganese oxide electrode, (4) PCTFE polymeric support, and (5) stainless steel holder with stainless steel pins for the lithium counter electrode. **(c)** Optical image of natural speckle pattern on the surface of the electrode used for DIC

H_2O levels both under 3 ppm. The cell was filled with approximately 5 mL electrolyte and sealed with the quartz window and an o-ring. The electrodes were analyzed by cyclic

voltammetry at scan rates of 25, 50 and 100 $\mu\text{V/s}$ against a lithium metal counter electrode using an potentiostat/galvanostat (Model LBT-21084, Arbin Instruments).

Strain in the electrode was measured by digital image correlation (DIC) following the method established by Jones et al. [14]. The natural speckle pattern of the composite electrode surface (Fig. 2(c)) was sufficient for correlation, and no additional patterning was necessary. During electrochemical cycling, the surface of the electrode was illuminated with white light. Images were acquired at every 2.5, 5 and 10 min when the electrodes were cycled at 100, 50 and 25 $\mu\text{V/s}$, respectively. The image exposure time was 2–5 s. A CCD camera (EXi Aqua, Q-imaging) equipped with a 12X zoom lens (Navitar) was used to capture images of a 2.5×3.5 mm region of interest (ROI) on a scale of $3.24 \mu\text{m}\text{-pixel}^{-1}$. The ROI is located between the two supports and approximately 1.0 mm away from the spot welds (Fig. 2(b)). The resolution of the images was 1392×1040 pixel and bit depth was 8. The free expansion and contraction of the electrode was characterized by calculating the normal strain in x direction (ϵ_{xx}) averaged over the ROI. Correlations to calculate displacements and strains were performed using the commercial software VIC2D using a subset size of $60 \mu\text{m}$ by $60 \mu\text{m}$. To calculate the noise level in the strain measurements, images were acquired during the open circuit period using a pristine electrode. The standard deviation was calculated by taking the square root of the variance in data and found to be less than 0.005%. An average of 223 strain data points were collected for each cycle, therefore strain data was collected for each 10 mV interval. Strain data were synchronized with electrochemical data using MATLAB (MathWorks® R2014b). Strain values were shifted to start from zero at the beginning of each delithiation cycle.

Impedance Measurements

Electrochemical impedance spectroscopy (EIS) was performed using standard CR2032 coin cells with a LMO cathode as the working electrode, a lithium metal anode as the counter electrode and a Celgard polyethylene separator. The impedance measurements were conducted using a VSP potentiostat equipped with acquisition software EC-lab®. EIS was performed in potentiostatic (PEIS) mode at different states of charge using 15 mV AC perturbation voltage of frequencies ranging from 0.01 Hz to 100 Hz. The desired state of charge (SOC) for EIS data acquisition was achieved by cycling between 3.5 V and 4.5 V, starting at the open circuit potential followed by delithiation at scan rate of 25 $\mu\text{V/s}$. The potential of the electrode was held at the SOC for 3 h before EIS.

Nyquist spectra were recorded after the electrode voltage became constant at the desired potential. The Nyquist impedance diagrams were computed by EIS data analysis software provided by EC-Lab®. A representative Nyquist plot is

shown in Fig. 3 for a LMO electrode after the first delithiation cycle until 3.9 V. The three main regions in the Nyquist plot are defined as the high, medium and low frequency regions. The semicircle in the high frequency region is related to surface resistance, R_s and capacitance, Q_s and provides information about Li^+ ion diffusion through the surface layer on the electrode surface. Charge transfer resistance between the surface layer and the active material, R_{CT} and the double layer capacitance, Q_{DL} are calculated from the semicircle in the medium frequency region. In the low frequency region, the straight line is associated with a Warburg type element (W) and provides information about the solid-state diffusion of Li^+ ions in the active material [41–43].

In order to compare the impedance measurements made in coin cells with the strain measurements made in our custom cell, pristine electrodes were used to measure the cell resistance for the two different cells using impedance spectroscopy. The potential for the coin cells was shifted with respect to the custom cell, such that $E_i = E + iR_{Cell}$, where E_i is the corrected (shifted) potential of the coin cell with respect to custom cell, E and i are the measured potential and current in coin cell and R_{Cell} is the cell resistance in the custom cell. The measured cell resistance accounts for the solution resistance and the contact resistance between the electrode and stainless steel.

Results and Discussion

The surface morphology of the LMO particles and LMO electrodes were analyzed using ESEM and profilometry. Figure 4 shows SEM images of LMO particles (no binder) and the LMO composite electrode. The average particle size was $2.60 \pm 1.2 \mu\text{m}$. The thickness of the free-standing LMO electrodes

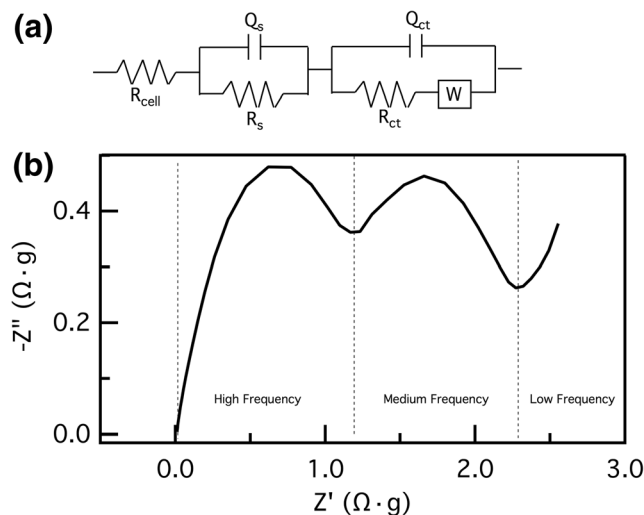


Fig. 3 Representative EIS data for an LMO cathode. (a) Equivalent circuit and (b) Nyquist plot during first delithiation at 3.9 V

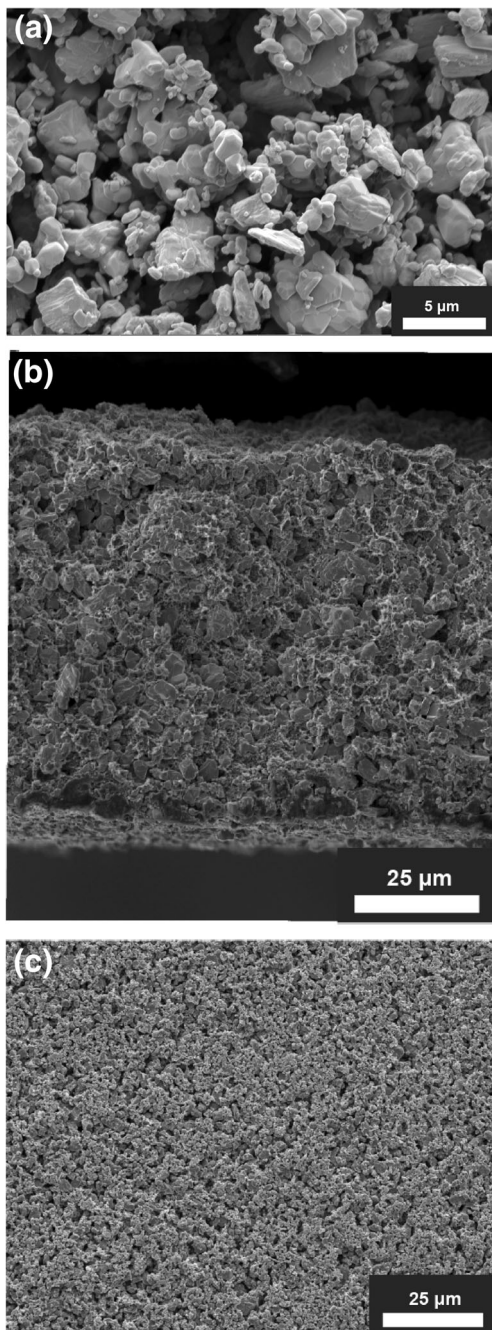


Fig. 4 Scanning electron microscopy images of (a) LMO particles, (b) cross-sectional composite LMO electrode and (c) surface of the composite LMO electrode

for strain measurements was $75 \pm 5 \mu\text{m}$. Figure 4(b), (c) reveal the homogeneous distribution of LMO particles in the composite electrode. Figure 5 shows a representative surface roughness profile across the center of the composite electrode. The RMS average surface roughness was $3.6 \pm 1.0 \mu\text{m}$ and was within the range of LMO particle size.

A composite LMO electrode was continuously cycled at $25 \mu\text{V/s}$ rate for six cycles. Figure 6 shows the current density (J) and strain (ϵ_{xx}) responses of the electrode. As expected for

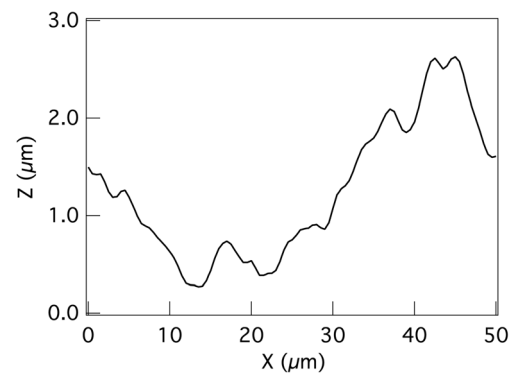


Fig. 5 Representative surface roughness line scan from the center region of the LMO composite electrode. Data was collected from the entire electrode and the average roughness was $3.6 \pm 1.0 \mu\text{m}$

LMO, two distinct peaks occur in the current density, labeled α and γ , during delithiation and they correspond to the phase transformations in the material. During lithiation, the corresponding phase transitions are labeled α' and γ' . The delithiation portion of the first cycle showed a very high current, compared to the subsequent cycles. As expected, the strain decreased during delithiation as Li^+ ions were removed from the electrode and increased during lithiation as Li^+ ions intercalated back into the electrode. The magnitude of the strain at the end of the first delithiation cycle (4.5 V) was

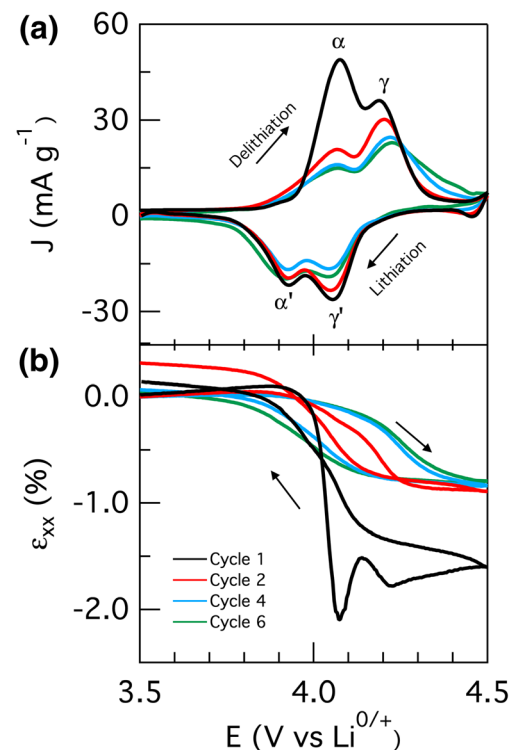


Fig. 6 Electrochemical and mechanical response of composite LMO electrode cycled at $25 \mu\text{V/s}$. (a) Current density and (b) strain evolution during cycle 1 (black line —), cycle 2 (red line —), cycle 4 (blue line —), and cycle 6 (green line —). Current peaks are labeled as α and γ during delithiation and α' and γ' during lithiation, respectively. Arrows indicate direction of the scans

significantly larger than after the second cycle and remaining nearly unchanged with subsequent cycles. At the end of the first cycle (at 3.5 V), the electrode did not return to its original size, resulting in 0.13% irreversible strain. The amount of irreversible strain during the second cycle increased to 0.30%, but then decreased in subsequent cycles and became less than 0.05% after cycle 6.

Figure 7 shows current density and strain response of a LMO composite electrode cycled at 100 $\mu\text{V/s}$ rate for eight cycles. Again, two distinct peaks were observed in the cyclic voltammetry, corresponding to the phase transformations. Similar to Fig. 6, the current density was much higher in the first cycle compared to subsequent cycles. The corresponding strain response is shown in Fig. 7(b). At this higher cycling rate, the magnitude of the strain at the end of delithiation (at 4.5 V) continuously decreased with cycle number. The value of the irreversible strain after the first cycle (-0.53%) also continuously decreased in subsequent cycles.

Strain Development During First Cycle

The irreversible strain in the electrode has been attributed to Mn^{2+} ion dissolution [27, 31], oxygen loss in the LMO particles [39, 40] and the formation of the CEI layer [7–9]. We

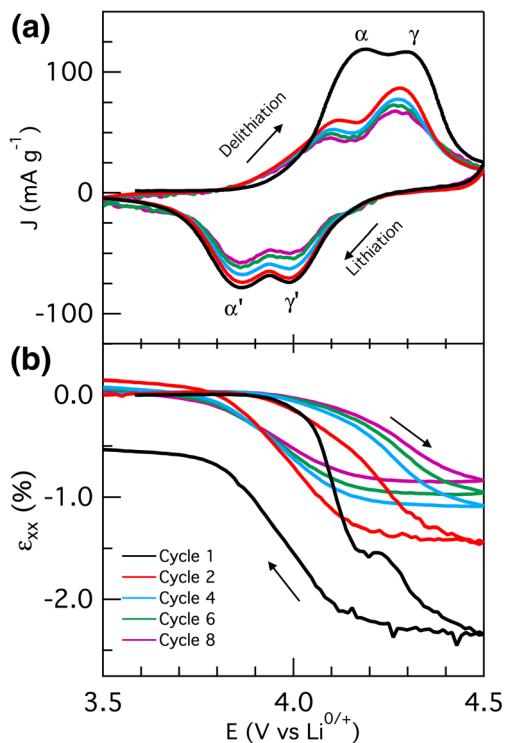


Fig. 7 Electrochemical and mechanical response of composite LMO electrode cycled at 100 $\mu\text{V/s}$. **(a)** Current density and **(b)** strain evolution during cycle 1 (black line \longrightarrow), cycle 2 (red line \longrightarrow), cycle 4 (blue line \longrightarrow), cycle 6 (green line \longrightarrow) and cycle 8 (purple line \longrightarrow). Current peaks are labeled as α and γ during delithiation and α' and γ' during lithiation, respectively. Arrows indicate direction of the scans

hypothesize that the changes in strain evolution during the first delithiation are primarily related to dynamic changes on the electrode surface. In the literature, the Faradaic current is defined as the current associated with surface reactions on the electrode surface and is estimated by subtracting the current measured in the second cycle from the first, $i_F = i(\text{cycle } 1) - i(\text{cycle } 2)$ [44, 45]. Similarly, we herein define a strain difference associated with the surface reactions during the first cycle, by subtracting the strain measured in the second cycle from the first, $\Delta\varepsilon_{xx} = \varepsilon_{xx}(\text{cycle } 1) - \varepsilon_{xx}(\text{cycle } 2)$.

The relationship between Faradaic current, strain difference and surface resistance are summarized in Fig. 8 for the slower scan rate (25 $\mu\text{V/s}$). Faradic current and strain difference are calculated using current and strain data in Fig. 6. Surface resistance (R_S) is extracted from EIS measurements and plotted for the first, second and third delithiation cycles. Characteristic changes in Faradaic current, strain difference and film resistance are divided into four stages, demarcated by the initiation of current flow, α phase transformation and the local minima in current between the α and γ peaks^[56–58].

During stage I, the Faradaic current and strain difference remain nearly constant. Interestingly, R_S values in this stage are similar with the R_S value of the pristine LMO, which is measured as $0.96 \Omega \cdot \text{g}$. In stage II after current begins to flow, the surface resistance decreases dramatically, the strain difference rapidly becomes more negative, and the Faradaic current increases to a maximum. After the α phase transformation (stage III), R_S increases slightly, the strain difference becomes less negative, and the Faradaic current starts to decrease. Finally in stage IV, the Faradaic current approaches zero, the strain difference slowly reaches a plateau value, and R_S becomes similar to the value measured in the later cycles.

The proposed mechanism for strain and film resistance evolution during the first delithiation cycle is shown schematically in Fig. 9. Native surface layers, mainly composed of Li_2CO_3 , already exist on the pristine LMO electrodes [8, 33]. The native surface layer remains persistent and stable during open circuit storage of the electrode in the electrolyte [35]. The initial stable surface resistance of the electrode in stage I in Fig. 8 is associated with the presence of native surface layer on the LMO surface. Interestingly, Chung et al. [45] observed a decrease in mass of the electrode, associated with surface film dissolution at the start of delithiation (stage II). We hypothesize that this removal of the native surface layers is correlated with the reduction in surface resistance and volume (increasingly negative strain) of the electrode measured during stage II in Fig. 8. Removal of the native surface layer may also enhance the dissolution of manganese due to direct contact between electrode and electrolyte [27, 31] and contribute to volumetric contraction of the electrode.

At higher potentials, the strain becomes less negative (indicating expansion) even though lithium ions are being removed from the electrode. Sheth et al. [39] observed an

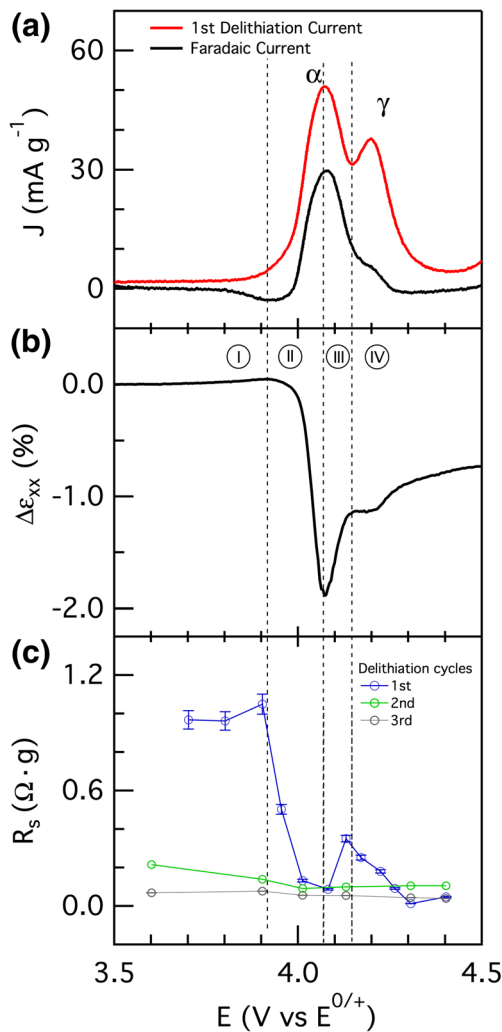


Fig. 8 Evolution of current density (J), strain difference ($\Delta\varepsilon_{xx}$) and surface resistance (R_s) evolution during the first delithiation cycle in LMO cycled at $25 \mu\text{V/s}$. (a) First delithiation current (red line \rightarrow) and Faradaic current (black line \rightarrow), (b) strain difference between first and second delithiation and (c) surface film resistance during first (blue line \oplus) and third (green line \oplus) delithiation. The faradic current and strain differences are calculated using current and strain data from the first and second delithiation cycles in Fig. 6. Characteristic changes in Faradaic current, strain difference and film resistance are divided into four stages. Vertical dashed lines divide these stages and correspond to initiation of current flow (start of stage II), α phase transformation (start of stage III) and local minimum in the current before the γ phase transformation (start of stage IV)

unexpected compressive stress generation during the later stages of the first delithiation of LMO thin films. They assumed that electrochemically induced oxygen vacancies can contribute to such irreversible stress evolution in the electrode. Chung et al. [45] reported an anomalous mass increase at the later stages of the first delithiation of LMO electrodes using electrochemical quartz crystal microbalance. They attributed the mass increase to the formation of solid-electrolyte interphase. Aurbach et al. [8, 35] showed that native surface layers are replaced by other surface species related to the

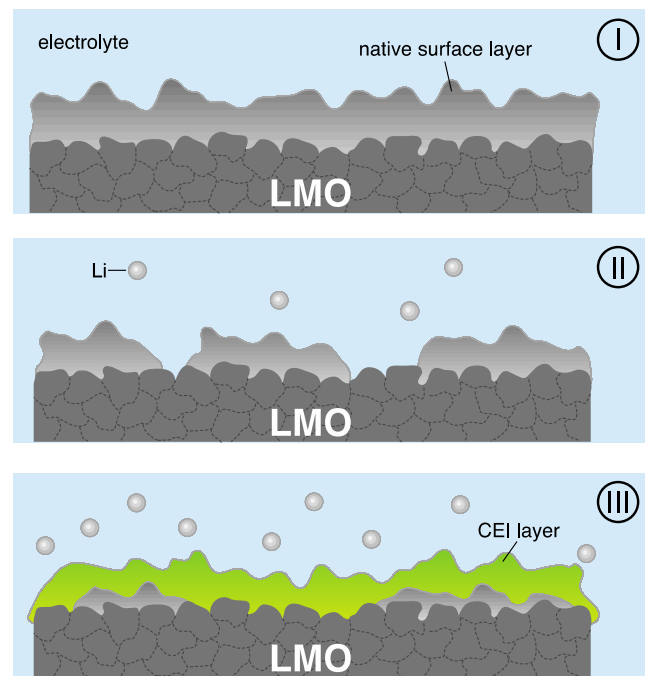


Fig. 9 Schematic representation of evolution of surface layer on LMO electrode during first delithiation cycle. Proposed mechanism related to surface layers. (I) Native surface layer on the surface of the pristine LMO electrode. (II) Dissolution of the native surface layer leads to reduction in the volume of the electrode. (III) Formation of the cathode-electrolyte interphase (CEI) layer on the surface of the LMO particles leads to increase in the volume of the electrode

decomposition of electrolyte components during the initial cycle. Manganese dissolution also takes place during electrochemical cycling and results into loss of active material. The formation of the new surface layer, manganese dissolution and oxygen vacancy generation may occur simultaneously, however only the formation of the surface layer can contribute to increase in mass and surface resistance. In the measurements reported in Fig. 8, we believe the formation of the CEI layer is manifested as the strain difference becoming less negative and a localized increase in surface resistance during stage III.

Strain development in the first delithiation cycle was also analyzed at different scan rates to better understand the role of current and applied potential. Figure 10 compares the Faradaic current and strain difference in the LMO electrode during the first delithiation at different scan rates. At the onset of the current flow (delithiation), Faradaic current begins to increase and the strain difference becomes more negative, both peaking at the α phase transition. Interestingly, the maximum change in strain difference for different scan rates does not occur at the same potential. Our measurements suggest that the change in strain in the first delithiation cycle (and potentially the dissolution of the native oxide layer) is triggered by current flow, rather than an applied potential. Strain differences continue to decrease until the α phase transition.

Figure 11 shows the total change in the strain difference during stages II and III with respect to square root of time.

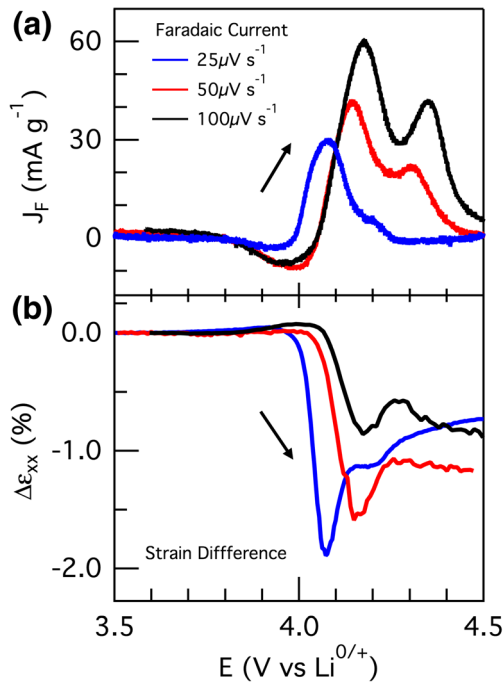


Fig. 10 Effect of scan rate on current and strain in LMO electrode during the first delithiation cycle. (a) Faradaic current density, J_F , and (b) strain difference, $\Delta\epsilon_{xx}$ at 25 $\mu\text{V/s}$ (blue line —), 50 $\mu\text{V/s}$ (red line —) and 100 $\mu\text{V/s}$ (black line —) scan rate. Arrows indicate direction of the scans

Changes in the strain difference for each stage are calculated by subtracting the value of strain difference at the beginning and end of each stage using data from the Fig. 10. The potential

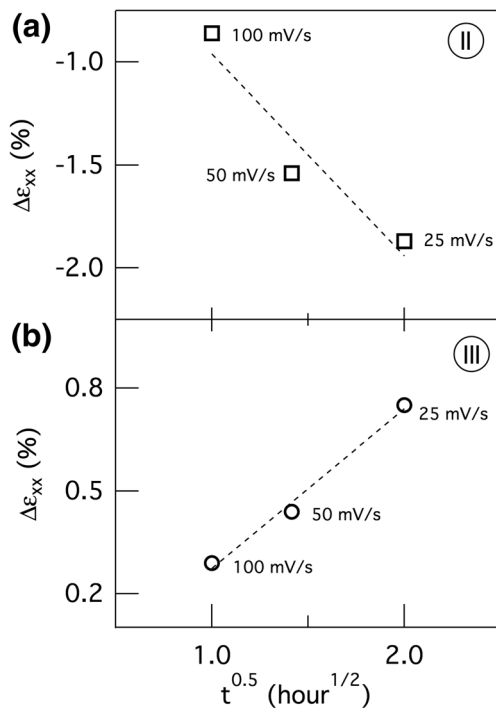


Fig. 11 Effect of scan rate on strain evolution during the first delithiation cycle. (a) Total change in strain difference as a function of square root of time during stage II and (b) during stage III potential zone (in Fig. 8)

change is divided by the corresponding scan rate in order to calculate total time elapsed during stages II and III at different scan rates. Figure 11(a) shows that the total strain developed during this period (stage II) is a linear function of the square root of time. After the α phase transition (stage III), the strain difference becomes less negative for all three scan rates. The total strain developed in stage III at each scan rate is plotted in Fig. 11(b) and also shows linear relationship with the square root of time. Jones et al. also observed a continuous increase in irreversible strain that was proportional to the square root of time that was associated with electrolyte decomposition on the surface of a composite graphite anode [6]. Simmen et al. [44] and Huang et al. [46] reported a square root time dependent surface layer formation on the electrode. Smith et al. attributed the time-dependent surface film formation on the graphite electrode to the diffusion of electrolyte components through the SEI layer [47]. Furthermore, Ploehn et al. developed a continuum mechanics model of solvent diffusion in the SEI layer that predicts a linear increase in surface layer thickness with the square root time [46]. Hence, the significant changes in strain associated with the first delithiation cycle are closely tied to critical electrochemical changes on the surface of the electrode and the formation of the CEI.

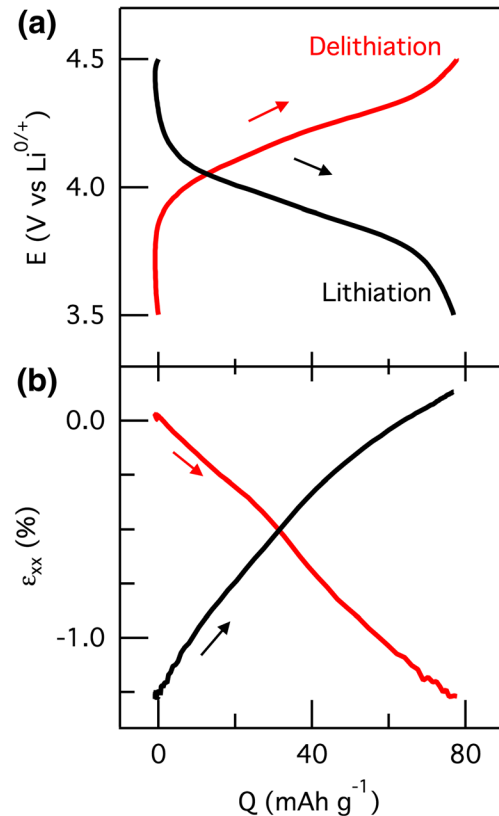


Fig. 12 (a) Representative voltage change and (b) strain as a function of capacity in the third cycle at 100 $\mu\text{V/s}$ during delithiation (red line —) and lithiation (black line —). Arrows indicate direction of the scans. Capacity is calculated by integrating the current data in Fig. 7(a) with respect to time. The corresponding strain data is also taken from Fig. 7(a)

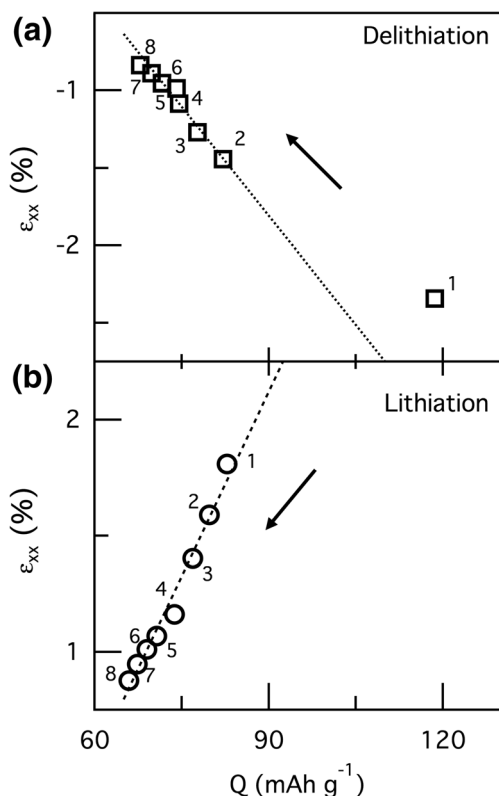


Fig. 13 Total amount of strain and capacity accumulated for each cycle during (a) delithiation and (b) lithiation in a LMO electrode cycled at $100 \mu\text{V/s}$. Numbers denote cycle number

Rate Effect on Strain Development

Beyond the first cycle, the magnitude of strain at the end of delithiation cycle and the current in the LMO electrode cycled at $25 \mu\text{V/s}$ (Fig. 6) does not change with cycle number significantly. In great contrast, the magnitude of strain at the end of delithiation cycle and the current in the electrode cycled at a faster rate of $100 \mu\text{V/s}$ continuously decrease with cycle number (Fig. 7). We examined the relationship between the electrode capacity and the change in strain at higher cycling rates. In Fig. 12, voltage and strain data for the third cycle are replotted as a function of a capacity in the LMO composite electrode cycled at $100 \mu\text{V/s}$. During delithiation, the capacity remains zero until the potential exceeds 3.8 V and then increases steadily (Fig. 12(a)). In contrast, the electrode contracts linearly with increasing capacity (Fig. 12(b)). Similarly during lithiation, the capacity remains zero until the voltage drops below 4.3 V , while the electrode expands uniformly with increasing capacity. We calculated the total amount of strain evolution associated with each delithiation and lithiation cycle and plot these as a function of capacity in Fig. 13. Except for the first cycle, the total strain change during delithiation decreased linearly with total capacity for each cycle (Fig. 13(a)). A similar

trend was observed for lithiation (Fig. 13(b)). The linear relationship between capacity and strain indicates that the cyclic volumetric changes in the electrode after the first cycle correlate with the amount of lithium inserted or removed from the LMO structure.

Both the strain and capacity decrease with increasing number of cycles, which can be attributed to Mn dissolution into the electrolyte and mechanical degradation of the electrode. The formation of HF acid and disproportion reactions at the particle surface contribute to the dissolution of manganese ions during cycling [32, 48]. Oh et al. showed that the manganese concentration in the electrolyte increases with the cycling number [49]. The number of available sites for lithium intercalation in the spinel structure decreases with manganese dissolution, resulting in capacity fade in the electrode. Mechanical damage such as particle debonding and/or cracking may also contribute to capacity fade in the electrode [19, 50]. Higher scan rates lead to a significant gradient of lithium ions in the active particles, which can generate large surface stresses and cause particle cracking and capacity fade [51, 52].

Conclusion

Digital image correlation was used to measure *in situ* strains in free-standing LMO composite electrodes cycled at different scan rates. Our measurements revealed the sensitivity of strain evolution to critical electrochemical changes at the surface of the electrode. Specifically, we observed the development of irreversible strain during the first delithiation cycle. The unique changes in strain during this first cycle were correlated with the dissolution of native surface layer and the formation of cathode-electrolyte interface layer. Strain data acquired at different scan rates suggested that current rather than the applied potential influences the dissolution of the native surface layer and the formation of CEI layer. In subsequent cycles, a large capacity fade was observed in the LMO electrodes cycled at high scan rates. Interestingly, the capacity fade scaled linearly with the maximum strain developed after each lithiation and delithiation cycle. Hence, our strain measurements suggest that control of the mechanical response of the electrode, i.e. strategies to reduce volumetric expansion, may have favorable effects on electrochemical performance.

Acknowledgements This work was supported as part of the Center for Electrochemical Energy Science, an Energy Frontier Research Center funded by the U. S. Department of Energy, Office of Science, Basic Energy Sciences. The authors would like to acknowledge the Beckman Institute for Advanced Science and Technology for use of microscopy equipment and Dr. Joseph Lyding for use of spot welding equipment.

References

- Tavassol H, Jones EMC, Sottos NR, Gewirth AA (2016) Electrochemical stiffness in lithium-ion batteries. *Nat Mater* 15: 1182–1187. <https://doi.org/10.1038/nmat4708>
- Çapraz ÖÖ, Bassett KL, Gewirth AA, Sottos NR (2016) Electrochemical stiffness changes in lithium manganese oxide electrodes. *Adv Energy Mater*:1601778–1601777. <https://doi.org/10.1002/aenm.201601778>
- Mukhopadhyay A, Sheldon BW (2014) Deformation and stress in electrode materials for li-ion batteries. *Prog Mater Sci* 63:58–116. <https://doi.org/10.1016/j.pmatsci.2014.02.001>
- Peled E, Golodnitsky D, Ardel G (1997) Advanced model for solid electrolyte interphase electrodes in liquid and polymer electrolytes. *J Electrochem Soc* 144:L208–L210. <https://doi.org/10.1149/1.1837858>
- Zhang S, Ding MS, Xu K et al (2001) Understanding solid electrolyte Interface film formation on graphite electrodes. *Electrochem Solid-State Lett* 4:A206–A208. <https://doi.org/10.1149/1.1414946>
- Jones EMC, Çapraz ÖÖ, White SR, Sottos NR (2016) Reversible and irreversible deformation mechanisms of composite graphite electrodes in lithium-ion batteries. *J Electrochem Soc* 163: A1965–A1974. <https://doi.org/10.1149/2.0751609jes>
- Vidu R, Quinlan FT, Stroeve P (2002) Use of in situ electrochemical atomic force microscopy (EC-AFM) to monitor cathode surface reaction in organic electrolyte. *Ind Eng Chem Res* 41:6546–6554. <https://doi.org/10.1021/ie020519z>
- Aurbach D (1998) Common electroanalytical behavior of li intercalation processes into graphite and transition metal oxides. *J Electrochem Soc* 145:3024–3034. <https://doi.org/10.1149/1.1838758>
- Das SR, Majumder SB, Katiyar RS (2005) Kinetic analysis of the li+ ion intercalation behavior of solution derived nano-crystalline lithium manganese thin films. *J Power Sour*. <https://doi.org/10.1016/j.jpowsour.2004.06.056>
- Beaulieu LY, Eberman KW, Tumer RL et al (2001) Colossal reversible volume changes in lithium alloys. *Electrochem Solid-State Lett* 4:A137–A140. <https://doi.org/10.1149/1.1388178>
- Liu XH, Huang JY (2011) In situ TEM electrochemistry of anode materials in lithium ion batteries. *Energy Environ Sci* 4:3844–3860. <https://doi.org/10.1039/c1ee01918j>
- Timmons A, Dahn JR (2006) In situ optical observations of particle motion in alloy negative electrodes for li-ion batteries. *J Electrochem Soc* 153:A1206–A1210. <https://doi.org/10.1149/1.2194611>
- Qi Y, Harris SJ (2010) In situ observation of strains during Lithiation of a graphite electrode. *J Electrochem Soc* 157:A741–A747. <https://doi.org/10.1149/1.3377130>
- Jones EMC, Silberstein MN, White SR, Sottos NR (2014) In situ measurements of strains in composite battery electrodes during electrochemical cycling. *Exp Mech* 54:971–985. <https://doi.org/10.1007/s11340-014-9873-3>
- Gonzalez J, Sun K, Huang M et al (2014) Three dimensional studies of particle failure in silicon based composite electrodes for lithium ion batteries. *J Power Sour* 269:334–343. <https://doi.org/10.1016/j.jpowsour.2014.07.001>
- Eastwood DS, Yufit V, Gelb J et al (2013) Lithiation-induced dilation mapping in a lithium-ion battery electrode by 3D X-ray microscopy and digital volume correlation. *Adv Energy Mater* 4: 1300506–1300507. <https://doi.org/10.1002/aenm.201300506>
- Wang H, Jang Il Y, Huang B et al (1999) TEM study of electrochemical cycling-induced damage and disorder in LiCoO₂ cathodes for rechargeable lithium batteries. *J Electrochem Soc* 146: 473–480
- Dokko K, Nishizawa M, Horikoshi S, Itoh T (2000) In situ observation of LiNiO₂ single-particle fracture during li-ion extraction and insertion. *Electrochem solid-state Lett* 3:125–127
- Zhang Z, Chen Z, Wang G et al (2016) Dual-doping to suppress cracking in spinel LiMn₂O₄: a joint theoretical and experimental study. *Phys Chem Chem Phys* 18:6893–6900. <https://doi.org/10.1039/c5cp07182h>
- Wang D, Wu X, Wang Z, Chen L (2005) Cracking causing cyclic instability of LiFePO₄ cathode material. *J Power Sour* 140:125–128. <https://doi.org/10.1016/j.jpowsour.2004.06.059>
- Julien, CM, Mauger A, Zaghbi K, Groult, H (2014) Comparative issues of cathode materials for Li-ion batteries. *Inorganics* 2:132–154. <https://doi.org/10.3390/inorganics2010132>
- Xu X, Lee S, Jeong S et al (2013) Recent progress on nanostructured 4 V cathode materials for li-ion batteries for mobile electronics. *Mater Today* 16:487–495. <https://doi.org/10.1016/j.mattod.2013.11.021>
- Hausbrand R, Cherkashinin G, Ehrenberg H et al (2015) Fundamental degradation mechanisms of layered oxide li-ion battery cathode materials: methodology, insights and novel approaches. *Materials Science & Engineering B* 192:3–25. <https://doi.org/10.1016/j.mseb.2014.11.014>
- Etacheri V, Marom R, Elazari R et al (2011) Challenges in the development of advanced li-ion batteries: a review. *Energy Environ Sci* 4:3243–3220. <https://doi.org/10.1039/c1ee01598b>
- Sun X, Yang XQ, Balasubramanian M et al (2002) In situ investigation of phase transitions of Li_{1+y}Mn₂O₄ spinel during li-ion extraction and insertion. *J Electrochem Soc* 149(7):A842. <https://doi.org/10.1149/1.1481523>
- Qi Y, Hector LG, James C, Kim KJ (2014) Lithium concentration dependent elastic properties of battery electrode materials from first principles calculations. *J Electrochem Soc* 161:F3010–F3018. <https://doi.org/10.1149/2.0031411jes>
- Edström K, Gustafsson T, Thomas JO (2004) The cathode–electrolyte interface in the li-ion battery. *Electrochim Acta* 50:397–403. <https://doi.org/10.1016/j.electacta.2004.03.049>
- Aurbach D, Levi MD, Gamulski K et al (1999) Capacity fading of LiMn₂O₄ spinel electrodes studied by XRD and electroanalytical techniques. *J Power Sour* 81:472–479
- Aurbach D, Talyosef Y, Markovsky B et al (2004) Design of electrolyte solutions for li and li-ion batteries: a review. *Electrochim Acta* 50:247–254. <https://doi.org/10.1016/j.electacta.2004.01.090>
- Aurbach D, Markovsky B, Salitra G et al (2007) Review on electrode–electrolyte solution interactions, related to cathode materials for li-ion batteries. *J Power Sour* 165:491–499. <https://doi.org/10.1016/j.jpowsour.2006.10.025>
- Eriksson T, Andersson AM, Bishop AG et al (2002) Surface analysis of LiMn₂O₄ electrodes in carbonate-based electrolytes. *J Electrochem Soc* 149:A69–A78. <https://doi.org/10.1149/1.1426398>
- Eriksson T, Gustafsson T, Thomas JO (2002) Surface structure of LiMn₂O₄ electrodes. *Electrochem Solid-State Lett* 5:A35–A34. <https://doi.org/10.1149/1.1432782>
- Xu K (2004) Nonaqueous liquid electrolytes for lithium-based rechargeable batteries. *Chem Rev* 104:4303–4418. <https://doi.org/10.1021/cr030203g>
- Chung KY, Yoon W-S, Kim K-B et al (2011) Formation of an SEI on a LiMn₂O₄ cathode during room temperature charge–discharge cycling studied by soft X-ray absorption spectroscopy at the fluorine K-edge. *J Appl Electrochem* 41:1295–1299. <https://doi.org/10.1007/s10800-011-0344-6>
- Aurbach D, Gamolsky K, Markovsky B et al (2000) The study of surface phenomena related to electrochemical lithium intercalation into lix MO_y host materials (M = Ni, Mn). *J Electrochem Soc* 147: 1322–1331. <https://doi.org/10.1149/1.1393357>



36. Tavassol H, Chan MKY, Catarello MG et al (2013) Surface coverage and SEI induced electrochemical surface stress changes during Li deposition in a model system for Li-ion battery anodes. *J Electrochem Soc* 160:A888–A896. <https://doi.org/10.1149/2.068306jes>
37. Wang JW, He Y, Fan F et al (2013) Two-phase electrochemical lithiation in amorphous silicon. *Nano Lett* 13:709–715. <https://doi.org/10.1021/nl304379k>
38. Paz-Garcia JM, Taiwo OO, Tudisco E et al (2016) 4D analysis of the microstructural evolution of Si-based electrodes during lithiation: time-lapse X-ray imaging and digital volume correlation. *J Power Sour* 320:196–203. <https://doi.org/10.1016/j.jpowsour.2016.04.076>
39. Nation L, Li J, James C et al (2017) In situ stress measurements during electrochemical cycling of lithium-rich cathodes. *J Power Sour* 364:383–391. <https://doi.org/10.1016/j.jpowsour.2017.08.006>
40. Sheth J, Karan NK, Abraham DP et al (2016) In situ stress evolution in $\text{Li}_{1+x}\text{Mn}_2\text{O}_4$ thin films during electrochemical cycling in Li-ion cells. *J Electrochem Soc* 163:A2524–A2530. <https://doi.org/10.1149/2.0161613jes>
41. Cho H-M, Chen MV, MacRae AC, Meng YS (2015) Effect of surface modification on Nano-structured $\text{LiNi}_{0.5}\text{Mn}_{1.5}\text{O}_4$ spinel materials. *ACS Appl Mater Interfaces* 7:16231–16239. <https://doi.org/10.1021/acsami.5b01392>
42. Ho C (1980) Application of A-C techniques to the study of lithium diffusion in tungsten trioxide thin films. *J Electrochem Soc* 127:343–350. <https://doi.org/10.1149/1.2129668>
43. Xie J, Kohno K, Matsumura T et al (2008) Li-ion diffusion kinetics in LiMn_2O_4 thin films prepared by pulsed laser deposition. *Electrochim Acta* 54:376–381. <https://doi.org/10.1016/j.electacta.2008.07.067>
44. Goonetilleke PC, Zheng JP, Roy D (2009) Effects of surface-film formation on the electrochemical characteristics of LiMn_2O_4 cathodes of lithium ion batteries. *J Electrochem Soc* 156:A709–A719. <https://doi.org/10.1149/1.3155432>
45. Zheng J, Sulyma C, Goia C et al (2012) Electrochemical features of ball-milled lithium manganate spinel for rapid-charge cathodes of lithium ion batteries. *J Solid State Electrochem* 16:2605–2615. <https://doi.org/10.1007/s10008-012-1677-8>
46. Ploehn HJ, Ramadass P, White RE (2004) Solvent diffusion model for aging of lithium-ion battery cells. *J Electrochem Soc* 151:A456–A462. <https://doi.org/10.1149/1.1644601>
47. Smith AJ, Burns JC, Zhao X et al (2011) A high precision Coulometry study of the SEI growth in Li/graphite cells. *J Electrochem Soc* 158:A447–A452. <https://doi.org/10.1149/1.3557892>
48. Lu CH, Lin SW (2002) Dissolution kinetics of spinel lithium manganate and its relation to capacity fading in lithium ion batteries. *J Mater Res*. <https://doi.org/10.1557/JMR.2002.0219>
49. Jang DH, Shin YJ, Oh SM (1996) Dissolution of spinel oxides and capacity losses in 4 V Li/Li_xMn₂O₄ cells. *J Electrochem Soc* 143:2204–2211. <https://doi.org/10.1149/1.1836981>
50. Miller DJ, Proff C, Wen JG et al (2013) Observation of microstructural evolution in Li battery cathode oxide particles by in situ electron microscopy. *Adv Energy Mater* 3:1098–1103. <https://doi.org/10.1002/aenm.201300015>
51. Cheng Y-T, Verbrugge MW (2008) The influence of surface mechanics on diffusion induced stresses within spherical nanoparticles. *J Appl Phys*. <https://doi.org/10.1063/1.3000442>
52. Zhao K, Pharr M, Vlassak JJ, Suo Z (2010) Fracture of electrodes in lithium-ion batteries caused by fast charging. *J Appl Phys* 108(7):073517. <https://doi.org/10.1063/1.3492617>